Publication Year	2024
Acceptance in OA	2025-03-07T13:20:56Z
Title	The SARAO MeerKAT 1.3 GHz Galactic Plane Survey
Authors	Goedhart, S., Cotton, W. D., Camilo, F., Thompson, M. A., UMANA, Grazia Maria Gloria, Bietenholz, M., Woudt, P. A., Anderson, L. D., BORDIU, Cristobal, Buckley, D. A.H., BUEMI, CARLA SIMONA, BUFANO, FILOMENA, CAVALLARO, Francesco, Chen, H., Chibueze, J. O., Egbo, D., Frank, B. S., Hoare, M. G., INGALLINERA, Adriano, Irabor, T., Kraan-Korteweg, R. C., Kurapati, S., LETO, PAOLO, LORU, Sara, Mutale, M., Obonyo, W. O., Plavin, A., Rajohnson, S. H.A., Rigby, A., RIGGI, Simone, Seidu, M., SERRA, Paolo, Smart, B. M., Stappers, B. W., Steyn, N., Surnis, M., TRIGILIO, CORRADO, Williams, G. M., Abbott, T. D., Adam, R. M., Asad, K. M.B., Baloyi, T., Bauermeister, E. F., Bennet, T. G.H., Bester, H., Botha, A. G., Brederode, L. R.S., Buchner, S., Burger, J. P., Cheetham, T., Cloete, K., de Villiers, M. S., de Villiers, D. I.L., du Toit, L. J., Esterhuyse, S. W.P., Fanaroff, B. L., Fourie, D. J., Gamatham, R. R.G., Gatsi, T. G., Geyer, M., Gouws, M., Gumede, S. C., Heywood, I., Hokwana, A., Hoosen, S. W., Horn, D. M., Horrell, L. M.G., Hugo, B. V., Isaacson, A. I., Józsa, G. I.G., Jonas, J. L., Jordaan, J. D.B.L., Joubert, A. F., Julie, R. P.M., Kapp, F. B., Kriek, N., Kriel, H., Krishnan, V. K., Kusel, T. W., Legodi, L. S., Lehmensiek, R., Lord, R. T., Macfarlane, P. S., Magnus, L. G., Magozore, C., Main, J. P.L., Malan, J. A., Manley, J. R., Marais, S. J., Maree, M. D.J., Martens, A., Maruping, P., McAlpine, K., Merry, B. C., Mgodeli, M., Millenaar, R. P., Mokone, O. J., Monama, T. E., New, W. S., Ngcebetsha, B.
Publisher's version (DOI)	10.1093/mnras/stae1166
Handle	http://hdl.handle.net/20.500.12386/36504
Journal	MONTHLY NOTICES OF THE ROYAL ASTRONOMICAL SOCIETY
Volume	531

Monthly Notices of the ROYAL ASTRONOMICAL SOCIETY

MNRAS **531,** 649–681 (2024) https://doi.org/10.1093/mnras/stae1166
Advance Access publication 2024 May 3

The SARAO MeerKAT 1.3 GHz Galactic Plane Survey

S. Goedhart [1,2★] W. D. Cotton [1,3] F. Camilo,[1★] M. A. Thompson,[4★] G. Umana,[5] M. Bietenholz [6,7] P. A. Woudt [8] L. D. Anderson,[9,10,11] C. Bordiu [5] D. A. H. Buckley [8,12,13] C. S. Buemi,[5] F. Bufano,[5] F. Cavallaro [5] H. Chen,[8,14] J. O. Chibueze [15,16,17] D. Egbo,[8,12] B. S. Frank,[1,8,18,19] M. G. Hoare [4] A. Ingallinera [5] T. Irabor,[4] R. C. Kraan-Korteweg,[8] S. Kurapati,[8] P. Leto [5] S. Loru,[5] M. Mutale,[4] W. O. Obonyo,[20] A. Plavin [3,21,22] S. H. A. Rajohnson [8] A. Rigby [4] S. Riggi [5] M. Seidu,[16] P. Serra,[23] B. M. Smart,[24,25] B. W. Stappers [26] N. Steyn [8,27] M. Surnis [28] C. Trigilio,[5] G. M. Williams [4,29] T. D. Abbott,[1] R. M. Adam,[1,30] K. M. B. Asad,[1,31] T. Baloyi,[1] E. F. Bauermeister,[1] T. G. H. Bennet,[1] H. Bester,[1] A. G. Botha,[1] L. R. S. Brederode,[1,30] S. Buchner,[1] J. P. Burger,[1] T. Cheetham,[1] K. Cloete,[1] M. S. de Villiers,[1] D. I. L. de Villiers,[32] L. J. du Toit,[33] S. W. P. Esterhuyse,[1] B. L. Fanaroff,[1] D. J. Fourie,[1] R. R. G. Gamatham,[1] T. G. Gatsi,[1] M. Geyer,[1,34] M. Gouws,[1] S. C. Gumede,[1] I. Heywood,[1,35,36] A. Hokwana,[1] S. W. Hoosen,[1] D. M. Horn,[1] L. M. G. Horrell,[1,37] B. V. Hugo,[1,36] A. I. Isaacson,[1] G. I. G. Józsa,[1,36] J. L. Jonas,[1,36] J. D. B. L. Jordaan,[1] A. F. Joubert,[1] R. P. M. Julie,[1] F. B. Kapp,[1] N. Kriek,[1] H. Kriel,[1] V. K. Krishnan,[1] T. W. Kusel,[1] L. S. Legodi,[1] R. Lehmensiek,[32,33] R. T. Lord,[1,2] P. S. Macfarlane,[1] L. G. Magnus,[1,2] C. Magozore,[1] J. P. L. Main,[1] J. A. Malan,[1] J. R. Manley,[1] S. J. Marais,[33] M. D. J. Maree,[1] A. Martens,[1] P. Maruping,[1] K. McAlpine,[1] B. C. Merry,[1] M. Mgodeli,[1] R. P. Millenaar,[1] O. J. Mokone,[1] T. E. Monama,[38] W. S. New,[1] B. Ngcebetsha,[1,36] K. J. Ngoasheng,[1] G. D. Nicolson,[1] M. T. Ockards,[1] N. Oozeer,[1,36,39] S. S. Passmoor,[1] A. A. Patel,[1] A. Peens-Hough,[1] S. J. Perkins,[1] A. J. T. Ramaila,[1,36] S. M. Ratcliffe,[1,40] R. Renil,[1] L. L. Richter,[1,36] S. Salie,[1] N. Sambu,[1] C. T. G. Schollar,[1] L. C. Schwardt,[1] R. L. Schwartz,[1] M. Serylak,[1,30,41] R. Siebrits,[1] S. K. Sirothia,[1,36] M. J. Slabber,[1] O. M. Smirnov,[1,36,42] A. J. Tiplady,[1] T. J. van Balla,[1] A. van der Byl,[1] V. Van Tonder,[1] A. J. Venter,[1] M. Venter,[1] M. G. Welz[1] and L. P. Williams[1]

Affiliations are listed at the end of the paper

Accepted 2024 April 25. Received 2024 April 25; in original form 2023 December 13

ABSTRACT

We present the SARAO MeerKAT Galactic Plane Survey (SMGPS), a 1.3 GHz continuum survey of almost half of the Galactic Plane ($251^\circ \leq l \leq 358^\circ$ and $2^\circ \leq l \leq 61^\circ$ at $|b| \leq 1^\circ.5$). SMGPS is the largest, most sensitive, and highest angular resolution 1 GHz survey of the plane yet carried out, with an angular resolution of 8 arcsec and a broad-band root-mean-square sensitivity of ∼10–20 μJy beam^{-1}. Here, we describe the first publicly available data release from SMGPS which comprises data cubes of frequency-resolved images over 908–1656 MHz, power-law fits to the images, and broad-band zeroth moment integrated intensity images. A thorough assessment of the data quality and guidance for future usage of the data products are given. Finally, we discuss the tremendous potential of SMGPS by showcasing highlights of the Galactic and extragalactic science that it permits. These highlights include the discovery of a new population of non-thermal radio filaments; identification of new candidate supernova remnants, pulsar wind nebulae and planetary nebulae; improved radio/mid-infrared classification of rare luminous blue variables and discovery of associated extended radio nebulae; new radio stars identified by Bayesian cross-matching techniques; the realization that many of the largest radio-quiet Wide-field Infrared Survey Explorer (WISE) H II region candidates are not true H II regions; and a large sample of previously undiscovered background H I galaxies in the Zone of Avoidance.

Key words: catalogues – Galaxy: general – radio continuum: ISM – radio continuum: stars – radio lines: galaxies.

★ E-mail: sharmila.goedhart@skao.int (SG); fernando@sarao.ac.za (FC); m.a.thompson@leeds.ac.uk (MAT)

1 INTRODUCTION

Our understanding of the physical processes within the Milky Way Galaxy has seen steady progress through a succession of multiwavelength surveys of the Galactic Plane (GP). These surveys have been increasingly sensitive and at higher angular resolution, taking full advantage of new observatories such as Visible and Infrared Survey Telescope for Astronomy (VISTA) and *Herschel* and/or upgrades to existing facilities such as the Jansky Very Large Array (JVLA). The end result is a rich archive of both imaging and spectroscopic data from radio to X-ray wavelengths that covers a large fraction of the Milky Way Galaxy (e.g. Grindlay et al. 2005; Carey et al. 2009; Schuller et al. 2009; Molinari et al. 2010; Hoare et al. 2012; Irabor et al. 2023).

Radio-wavelength surveys are particularly powerful as the Galaxy is largely optically thin in the radio which means that we can study objects across (or even beyond) the Galaxy regardless of Galactic latitude. Moreover, radio photons are emitted via a range of physical processes (thermal brehmsstrahlung, synchrotron or gyro-synchrotron, recombination lines, rovibrational lines, and hyperfine transitions) which enable us to study many different astrophysical environments in main sequence (MS) and evolved stars, young stellar objects, H II regions, supernova remnants (SNRs), and all phases of the interstellar medium (ISM) from ionized to molecular (e.g. Thompson et al. 2015; Umana et al. 2015a).

Recent radio surveys such as the Co-Ordinated Radio 'N' Infrared Survey for High-mass star formation (CORNISH; Hoare et al. 2012), CORNISH-South (Irabor et al. 2023), the GLObal view on STAR formation in the Milky Way (GLOSTAR; Brunthaler et al. 2021), the HI, OH, Recombination line survey of the Milky Way (THOR; Beuther et al. 2016), the Methanol Multi-Beam survey (Green et al. 2009), the Galactic and Extra-Galactic All-Sky MWA Survey (GLEAM; Hurley-Walker et al. 2019a), and the Stellar Continuum Originating from Radio Physics In Our Galaxy survey (SCORPIO; Umana et al. 2015b) have given insights into the Galactic star formation rate (Wells et al. 2022), identified new planetary nebulae (PNe) and SNRs (Fragkou et al. 2018; Ingallinera et al. 2019; Hurley-Walker et al. 2019b; Dokara et al. 2021), enabled the assembly of complete samples of ultracompact (UC) and compact H II regions (Kalcheva et al. 2018; Urquhart et al. 2018; Djordjevic et al. 2019), underpinned the discovery of new variable 6.7 GHz methanol masers (Maswanganye 2017) and revealed new optically thick hypercompact H II regions (Yang et al. 2019). The key features of these surveys are their high angular resolution (∼2–20 arcsec) and sensitivity (∼0.1–2 mJy in continuum 1σ). This range of angular resolution is comparable to that in visible to far-infrared (IR) surveys e.g. the Isaac Newton Telescope (INT) Photometric Hα Survey of the Northern Galactic Plane (IPHAS), the VST Photometric Hα Survey of the Southern Galactic Plane and Bulge (VPHAS+), the Galactic Legacy Infrared Midplane Survey Extraordinaire (GLIMPSE), and the Herchel Infrared Galactic Plane Survey (Hi-GAL), which enables straightforward multiwavelength analyses. Milli-Jansky sensitivity is crucial to trace the bulk of the population of Galactic massive star formation regions via compact and UC H II regions that were the primary targets of CORNISH, CORNISH-South, and GLOSTAR.

One limitation that applies to many of the interferometric surveys mentioned above is that to cover a wide area in a reasonable length of observing time places constraints on the Fourier-transform plane, or *uv*, coverage of the observations with resulting effects on image fidelity and dynamic range. This can be particularly apparent at low frequencies (∼1 GHz) where the increased brightness of non-thermal Galactic and extragalactic sources places dynamic range limitations on surveys. For this and other reasons, there is a significant gap in the coverage of the Milky Way at GHz frequencies, particularly in terms of angular resolution and sensitivity. In Quadrant I the deepest survey at 1–2 GHz is the THOR survey (Beuther et al. 2016), which has an angular resolution of ∼20 arcsec and a 1σ point-source sensitivity of ∼0.4 mJy beam^{-1} in a 128 MHz spectral window (Bihr et al. 2016). Similarly, in Quadrant IV, the Molonglo Galactic Plane Survey at 843 MHz has an angular resolution of 45 arcsec and a 1σ point-source sensitivity of ∼1 mJy beam^{-1}. More recently, the Rapid ASKAP Continuum Survey (RACS; McConnell et al. 2020) has observed the GP as part of its all-sky survey programme with an angular resolution of 10–47 arcsec (dependent on declination) and median sensitivity of 0.2 mJy PSF^{-1} at 1357 MHz (Duchesne et al. 2023). 887 MHz RACS data are also available, although the GP has not been catalogued due to source complexity (Hale et al. 2021).

Going beyond these limitations is crucial for understanding the non-thermal radio populations within the Milky Way, especially stellar radio sources (Umana et al. 2015a) and compact, potentially young SNRs (Gerbrandt et al. 2014; Ranasinghe, Leahy & Stil 2021). Moreover, since constrained *uv* coverage also results in limited image fidelity as well as dynamic range, our knowledge of extended low surface-brightness populations (e.g. H II regions and old SNRs) is also affected. Indeed, the power of new facilities with dense instantaneous *uv* coverage is exemplified in the MeerKAT Galactic Centre image (Heywood et al. 2022) which revealed both the striking complexity of this region and new populations of previously undiscovered radio sources.

It is with these goals in mind that we present the SARAO (South African Radio Astronomy Observatory) MeerKAT Galactic Plane Survey (SMGPS), an 8 arcsec angular resolution, ∼10–20 μJy beam^{-1} root-mean-square (RMS) sensitivity, 1.3 GHz survey of almost half of the GP. The SMGPS was designed to cover the bulk of Galactic radio emission and to exploit the tremendous capabilities of the MeerKAT array to explore the 1 GHz radio population with hitherto unavailable sensitivity, angular resolution, and image fidelity. SMGPS is primarily a continuum imaging survey using the 4096-channel continuum correlator mode of MeerKAT. However, this spectral resolution also makes extragalactic H I studies feasible, as shown in Section 6.

SMGPS is distinguished from the MPIfR-MeerKAT Galactic Plane Surveys (MMGPS; Padmanabh et al. 2023), which uses the subsequently developed commensal observing mode of MeerKAT to feed simultaneous pulsar search and imaging pipelines. The MMGPS *L*-band survey (MMGPS-L) is broadly similar to SMGPS in imaging terms, but shallower, with poorer *uv* coverage, and covering a wider range of Galactic latitudes ($|b| < 5.^{\circ}2$ versus $|b| < 1.^{\circ}5$) and a narrower range of Galactic longitudes ($260^{\circ} \leq l \leq 345^{\circ}$ versus $251^{\circ} \leq l \leq 358^{\circ}$ and $2^{\circ} \leq l \leq 61^{\circ}$). Together the two surveys are highly complementary, not least for variability studies with a multiyear baseline between the two surveys, but also as pathfinders to design and optimize future Square Kilometre Array observations.

In this paper, we present the survey, including the initial SMGPS data release (DR) and some science highlights, describing the observations in Section 2, the calibration, imaging, and mosaicing procedures in Section 3, and the principal data products and a through assessment of their quality in Section 4. In Section 5, we present a selection of the Galactic science highlights of the SMGPS, paying particular attention to areas where the SMGPS data makes a unique contribution to the state of the art. This includes the discovery of a new population of radio filaments (Section 5.1), new candidate SNRs (Section 5.2), new potential pulsar-wind nebulae of youthful pulsars (Section 5.3), PNe (Section 5.4.1), and radio stars (Section 5.5). In

Section 6, we describe the re-analysis of the SMGPS data to identify and study H I galaxies in the Zone of Avoidance (ZoA). Finally, in Section 7, we present a summary and conclusions.

2 OBSERVATIONS

The observations were carried out with the 64-antenna MeerKAT array in the Northern Cape Province of South Africa, which is described in Jonas & MeerKAT Team (2016), Camilo et al. (2018), and Mauch et al. (2020). The survey area was chosen to cover two contiguous blocks in Galactic longitude of $251^\circ \leq l \leq 358^\circ$ and $2^\circ \leq l \leq 61^\circ$. Each block covers a Galactic latitude range of approximately $|b| \leq 1.^\circ5$, with the first block chosen to follow the Galactic warp in a similar manner to the Hi-GAL survey (Molinari et al. 2010). The SMGPS survey area is shown in Fig. 1 with individual pointing centres represented as circles. The Galactic Centre was not observed as part of this survey, being instead observed separately and described in Heywood et al. (2022).

The SMGPS observations were made between 2018 July 21 and 2020 Mar 14 using the *L*-band receiver system, covering a frequency range 856–1712 MHz with 4096 channels, and an 8 s correlator integration period. The correlated data consist of all four combinations of the two orthogonal linearly polarized feeds. The observations were executed over a series of ∼10 h sessions, cycling among 9 pointings of a hexagonal grid spaced by $0.^\circ494$ to provide uniform sensitivity. Each pointing was visited multiple times over the session, providing good *uv* coverage and an on-source time of ≈1 h per pointing. The individual pointings were then formed into mosaics, extending to $|b| = 1.^\circ5$, having full sensitivity to $|b| \approx 1.^\circ2$, and slightly reduced beyond (for the warp-offset fields these latitude ranges are shifted southwards by $0.^\circ5$).

Observations in the fourth quadrant were initially chosen to have scan durations of 3 min per pointing, with a complex gain calibrator observed every 30 min for 65 s. Later observed scans for each pointing were extended to 10 min. The bandpass and flux calibrators PKS B1934 − 638 or PKS J0408 − 6545 were observed for five minutes every 3 hours. The polarization calibrator 3C 286 was observed for some sessions, when visible to the MeerKAT array. Typically at least 60 antennas were online for each session. A few observations were split into multiple sessions due to scheduling constraints.

Since these data were taken during an active development and commissioning stage of the MeerKAT array, a number of instrumental and calibration issues were found to affect the quality of different subsets of the observations. The main effects combine to result in systematic errors in the astrometry of the data at around the arcsecond level. We have corrected the astrometry errors as much as possible in our data reduction and post processing (see Section 4.4 for a full discussion of the astrometric accuracy of the processed data), but we describe the underlying instrumental issues here so that users fully understand the limitations of the survey data.

The earliest data taken had a labelling error of 2 s in time and a half channel in frequency, resulting in incorrectly calculated *u*, *v*, and *w* baseline coordinates. These errors result in rotated and mis-scaled images with apparent position errors of up to to 2 arcsec at the edge of each pointing. After the discovery of the labelling errors, subsequent data were corrected but earlier data were not. The affected data lie in the fourth quadrant between $l = 320^\circ$ and 358° (mosaics G321.5 to G357.5 – in this paper we refer to mosaics by their centre longitude). The labelling errors are mitigated to some extent by the mosaicing process carried out in the data reduction. The mosaics place low weight on the outer parts of the pointing images and so the labelling errors are only a significant contribution at the extremes of Galactic latitude covered by the survey where the mosaics are dominated by single pointings.

A second source of astrometric error was discovered in the initial MeerKAT calibrator list, which included calibrators with position errors of up to several arcseconds. This resulted in a constant positional offset in the pointings to which these calibrators were applied. The offset was corrected by modifying the reference pixel of the World Coordinate System of the affected pointings prior to the mosaicing process.

Finally, a more subtle problem resulted from the low accuracy of the correlator model used in the delay tracking of the observations. An insufficient number of mostly Earth orientation terms were included in the model. In order to get calibrators that dominate the field of the MeerKAT antennas, many were 10° or more from the target pointing, which can result in constant position offsets of up to several arcseconds in the target-pointing images. Since nearby regions of the GP used the same calibrator these errors will be spatially correlated. We have not applied a correction for this potential offset, but as will be seen in Section 4.4 we do not see a substantial error in the astrometric accuracy of the survey data.

3 DATA REDUCTION

The observational data were calibrated and imaged with a simple and straightforward procedure as described in Mauch et al. (2020) and Knowles et al. (2022). All calibration and imaging used the OBIT package[1] (Cotton 2008). We describe the calibration, imaging, and mosaicing process in the following subsections.

3.1 Calibration and editing

Data affected by interference and/or equipment malfunctions were identified using the procedures outlined in Mauch et al. (2020) and were removed from further analysis. The remaining data were calibrated for group delay, bandpass and amplitude, and phase as described in Knowles et al. (2022). The reference antenna was picked on the basis of the best signal-to-noise ratio, S/N, in the bandpass solutions. The flux-density scale is based on the Reynolds (1994) spectrum of PKS B1934 − 638:

$$\log(S) = -30.7667 + 26.4908\left(\log \nu\right) - 7.0977\left(\log \nu\right)^2 + 0.605334\left(\log \nu\right)^3, \quad (1)$$

where *S* is the flux density in Jy and ν is the frequency in MHz. After small time and frequency offsets were discovered (see Section 2), subsequent data sets were corrected before imaging. From long-term observatory monitoring of calibrators, the flux-density calibration uncertainty is believed to be ∼5 per cent.

3.2 Imaging

Individual pointings were imaged with the wide-band, wide-field OBIT imager MFImage (Cotton 2019). Each individual pointing was gridded in the J2000 FKS equatorial coordinate system. MFImage corrects for the curvature of the sky using facets. Multiple frequency bins were imaged independently and CLEANed jointly to accommodate the frequency dependencies of the sky brightness distribution and the antenna gains. A resolution of 7.5–8 arcsec,

[1] http://www.cv.nrao.edu/~bcotton/Obit.html

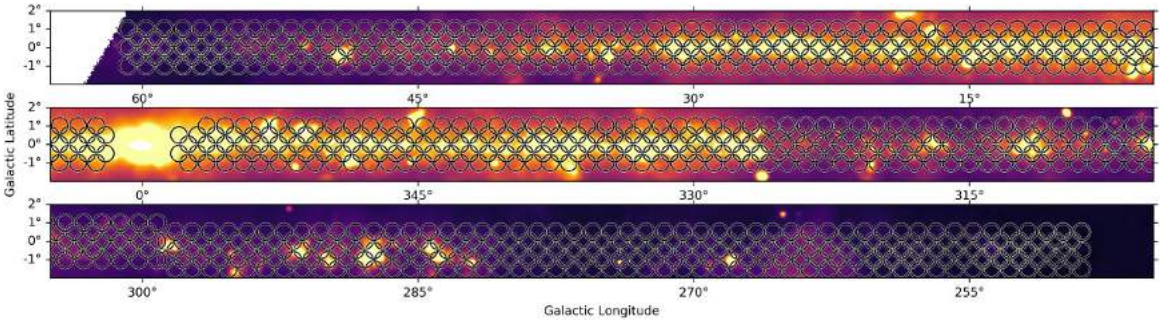

Figure 1. The area of the GP covered by the SMGPS. Individual pointing centres are shown by circles, overlaid on a single-dish 1.4 GHz continuum image from the HI Parkes All-Sky Survey (CHIPASS; Calabretta, Staveley-Smith & Barnes 2014).

nearly independent of frequency, was obtained using a frequency dependent taper.

For each pointing, the sky within 0.°8–1° radius was fully imaged with outlying facets to cover bright sources from the SUMMS 843 MHz catalogue (Mauch et al. 2003) within 1.°5 of the pointing centre. Two iterations of 30 s solution-interval phase-only self calibration were used. Amplitude and phase self-calibration were added as needed. The final Stokes *I* CLEAN used 250 000 CLEAN components with a loop gain of 0.1 and CLEANed typically to a depth of 100–200 μJy beam^{-1}. No direction dependent corrections were applied. Robust weighting (−1.5 in AIPS/OBIT usage) was used to down weight the very densely sampled inner portion of the *uv* coverage. The resulting resolution, as mentioned, was in the range 7.″5–8.″0. Imaging was done using 14 channel images each with 5 per cent fractional bandwidth.

A small number of mosaics were also processed with polarization calibration as described in Knowles et al. (2022) and Plavin, Cotton & Mauch (2020). This calibration used 3C 286 as a polarized calibrator, and PKS B1934 − 638 as an unpolarized one, and involved jointly solving for the polarization of the session complex gain calibrator and the instrumental polarization parameters using all calibrators. This calibration was applied to the data for which individual pointings were imaged in Stokes *I*, *Q*, *U*, and *V* and formed into mosaics as the rest of the survey was. Although the initial survey observations were not specifically designed with polarization calibration in mind, the instrumental stability of the MeerKAT system means that it is possible to recover the polarization calibration from initial noise injections performed at the start of each observation. For those tiles that were processed, Stokes *I*, *Q*, *U*, and *V* mosaics are included in the DR presented in this paper to demonstrate the potential of a future DR with full polarization calibration.

All four polarization products are available in the raw data for all pointings, it is only due to computational limitations that we only calibrated a small subset of the data for polarization. As an example of what is possible, we show in Appendix A images from a single pointing centred approximately on the SNR W44, which was recalibrated for polarization.

The dynamic range can be limited by very strong sources (> few hundred mJy beam^{-1}), especially if several are present in a given pointing. The self-calibration applied cannot correct for direction-dependent gain effects (DDEs), which may be the cause of some of the remaining artefacts seen in the individual images. The DDEs are thought to be dominated by pointing errors, asymmetries in the antenna pattern, and ionospheric refraction. For images that are not dynamic range limited, the off-source RMS brightness is ∼10–15 μJy beam^{-1}.

MeerKAT has extensive short baseline coverage allowing the imaging of extended emission. However, there is a minimum baseline length, which in wavelengths is frequency dependent; more extended emission is recovered at lower frequencies than higher ones. Regions of bright extended emission which are not well sampled by the *uv*-coverage will have negative bowls surrounding them. These bowls will be deeper at higher frequencies introducing an artificial steepening of the apparent spectrum. Angular scales up to 10 arcmin are generally well recovered although the estimate of the spectral index may be considerably in error and care must be taken to derive accurate spectral indices from the data. We discuss the inherent limitations of spectral indices derived from the data in Section 4.5.

3.3 Mosaics

The individual pointing images were collected into linear 3° × 3° mosaics. To allow convenient cross-comparisons with other GP surveys the mosaics were gridded on the IAU 1958 Galactic coordinate system. The mosaic formation process for each image plane is given by the summation over overlapping pointing images:

$$M(x, y, \nu) = \frac{\sum_{i=1}^{n} A_{i,\nu}(x, y)\, I_{i,\nu}(x, y)}{\sum_{i=1}^{n} A_{i,\nu}^{2}(x, y)}, \quad (2)$$

where $A_{i,\nu}(x, y)$ is the array gain of pointing i in direction (x, y) and at frequency ν, $I_{i,\nu}(x, y)$ is the pointing i pixel value interpolated to direction (x, y) in frequency plane ν, and M is the mosaic cube.[2] Quality checks were applied to each frequency plane of each pointing before being added to the mosaic; frequency planes with more than 50× the mean RMS were excluded from the mosaic. The images of the individual pointing were convolved to 8 arcsec FWHM (full width at half-maximum) resolution before combining into mosaics.

As part of the mosaic formation process a correction was applied for the primary antenna beam shape as part of the weighting of overlapping pointing images. The shape of the individual antenna power pattern is reasonably well understood although the array's effective power pattern is less so. Although array effective beam studies in Mauch et al. (2020) show that the inner beam is very close to that of an individual antenna, application of this pattern in Knowles et al. (2022) further out in the beam results in physically implausible spectra. The effect is similar to that expected from the known pointing errors of the antennas in the array. The primary beam corrections are not thought to be accurate past a radius of ∼36 arcmin. This region of the beam is given a low weight in the mosaic formation so the

[2]Note that the antennas have already applied one power of the antenna gain to the sky during the observations.

mosaics should not be adversely impacted by errors in the assumed array beam pattern except possibly for the extreme values in latitude which are dominated by data far from the nearest pointing centre.

4 SMGPS DATA RELEASE

With the publication of this paper we make available the first DR (DR1) of the SMGPS. DR1 consists of mosaiced data cubes assembled from the individual pointings, and 'zeroth-moment' integrated intensity images derived from the mosaics. The data cubes and images are presented in a common $3^\circ \times 3^\circ$ format with 7500×7500 pixels of $1\farcs5$ each. Fig. 2 presents an example of one of the mosaics (G342.5), combining a MeerKAT 1.3 GHz Moment 0 image with *Herschel* Hi-GAL 70 μm and 250 μm images to illustrate the thermal and non-thermal emission present in the image. Fig. 2 reveals a multitude of complex and striking emission on multiple angular scales, from large SNRs and H II regions to compact radio galaxies.

Advanced data products will be published separately and include catalogues of compact point-like, extended, and filamentary sources. All DR1 data products are available through a DOI,[3] and the raw visibilities are also hosted on the SARAO Data Archive[4] under project code SSV-20180721-FC-01.

Here, we describe the individual data products in DR1 (Sections 4.1 and 4.2), discuss the accuracy of the flux-density calibration (Section 4.3) and astrometry (Section 4.4), and the limitations of in-band spectral indices (Section 4.5).

4.1 Data cubes

As mentioned, the standard data product is a set of $3^\circ \times 3^\circ$ overlapping FITS mosaics, assembled from the individual pointing images as described in Section 3.3. Two versions of the Stokes *I* mosaics are included in DR1: (1) cubes containing observed flux densities for each of the 14 frequency planes described in Section 3.2 and Table 1; and (2) fitted parameter cubes, containing planes of broadband flux density, spectral index and their associated errors, obtained using a power-law fit to the frequency planes (described below). For the Stokes *Q*, *U*, and *V* mosaics, only the first of these are provided.

The data format of the frequency plane cubes is that outputted by MFImage and is described in detail in OBIT Memo 63.[5] In brief, the frequency plane cubes contain 16 data planes comprising a weighted average flux-density plane at an effective frequency of 1359.7 MHz, a spectral index plane, and each of the individual frequency planes in order of increasing frequency. The central frequencies and bandwidths of each of the frequency planes are given in Table 1. Since the steep spectrum Galactic emission contributes a significant portion of the system temperature, the weighting used in the broad-band flux-density plane was by 1/RMS of the frequency plane off-source background RMS brightness rather than the more usual $1/\mathrm{RMS}^2$. The weights used were the average RMS values over all mosaics (scaled to the overall RMS in each mosaic). This weighting results in an effective frequency of 1359.7 MHz.

The first two planes of the fitted parameter cubes, broad-band flux density at 1359.7 MHz and spectral index (Stokes *I* only), α, are identical to the first two planes of the frequency plane cubes described above. We use the $S_\nu \propto \nu^\alpha$ definition of α. Values of α were obtained by fitting by nonlinear least squares to each frequency plane of the frequency plane cubes using the weighting used for Stokes *I*. This fitting was done only for pixels with at least 500 μJy beam^{-1} of broad-band Stokes *I*, with the remainder being blanked. The resulting fitted values of α were accepted if the addition of α in the fit did not increase the χ^2 per degree of freedom, with any pixels failing this criterion also blanked. The third plane contains the error estimate for the broad-band flux-density plane. The fourth and fifth planes are the least-squares error estimate and χ^2 of the spectral index fit. These planes are blanked for pixels with no valid spectral index.

To maintain a fixed effective frequency and consistent spectral index fit, the 1359.7 MHz flux density and spectral index values have been calculated only for those pixels containing information in the highest frequency plane (i.e. channel 14 at 1656 MHz). As the primary beam FWHM reduces with increasing frequency, outlying parts of the mosaics do not contain data across the full range of frequencies (a graphical explanation of this is shown in Fig. 3).

The file name convention for the frequency plane cubes is <pos> I_Mosaic.fits where <pos> is the Galactic coordinate of the centre of the mosaic, for example, G339.5 + 000. The mosaics with polarization calibration additionally include separate frequency plane cubes for *Q*, *U*, and *V* with 'Q', 'U', or 'V' substituted for 'I' in the file name. Frequency plane cubes with fixed timing and labelling errors (Section 2) are denoted as IFx instead of I; all polarized products are corrected. The fitted parameter cubes are named as <pos>I_refit.fits, with again Fx denoting cubes with fixed timing and labelling errors.

4.2 Zeroth moment images

In addition to the data cubes discussed in the previous section we also make available zeroth moment integrated intensity images. The rationale behind these images is to provide an easily accessible standard FITS data product that encompasses the largest possible sky area. As described in Section 4.1, the weighted average Stokes *I* plane contained within the data cubes is computed only for pixels where there is a measurement in the highest frequency plane images. The large difference in the primary beamwidth between the lowest and highest frequencies observed by MeerKAT means that the Stokes *I* plane presented in the survey data cubes misses the extremes in Galactic latitude that were only observed at the lower frequencies.

The zeroth moment images were calculated on a pixel-by-pixel basis by summing the product of the flux density and bandwidth in each fractional bandwidth image, which was then weighted by the total bandwidth of all the fractional bandwidth images. The zeroth moment M_0 is then given by

$$M_0 = \frac{\sum_i S_i \Delta\nu_i}{\sum_i \Delta\nu_i}, \tag{3}$$

where S_i and $\Delta\nu_i$ are the flux density and bandwidth of each pixel in frequency plane *i*. This represents a bandwidth-weighted integrated intensity over all available pixels in each frequency plane in the frequency plane cubes. We note in passing that this is the astronomical definition[6] of moment zero as integrated intensity

[3] https://doi.org/10.48479/3wfd-e270. When using DR1 products, this paper should be cited, and the MeerKAT telescope acknowledgement included.
[4] https://archive.sarao.ac.za/
[5] https://www.cv.nrao.edu/~bcotton/ObitDoc/MFImage.pdf

[6] The astronomical definition of image moments is 'off-by-one' compared to the mathematical definition of moments, for example, https://casa.nrao.edu/docs/casaref/image.moments.html

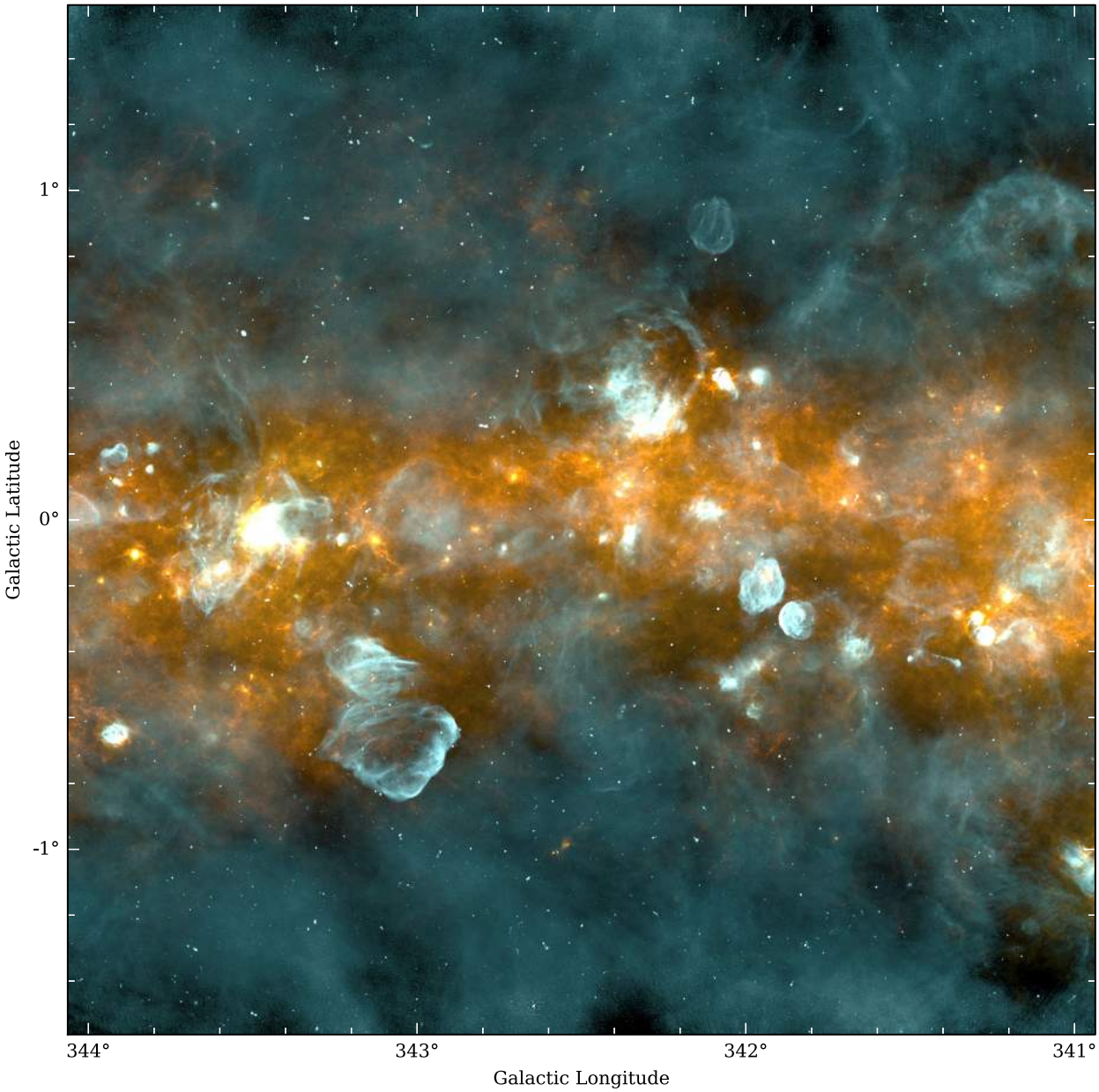

Figure 2. An example Moment 0 mosaic from SMGPS DR1. The image is a combination of SMGPS 1.3 GHz (white, blue, and cyan, which encode bright, mid-range, and low brightnesses, respectively) and *Herschel* Hi-GAL 70 μm (yellow) and 250 μm (orange) emission. This colour combination was chosen to differentiate between SNRs and H II regions; the former appear mostly cyan whereas the latter appear with white cores surrounded by yellow/orange emission.

($\int S\,\mathrm{d}\nu$) as opposed to the mathematical definition as the mean ($<S>$). As the zeroth moment images are derived from the data cubes described in Section 4.1, they have the same world coordinate system and size (i.e. $3^\circ \times 3^\circ$).

Pixels that were flagged (e.g. because they lie outside the imaged area or are affected by Radio Frequency Interference - RFI) do not contribute to the zeroth moment. It is important to note that as each pixel in the zeroth moment can contain contributions from different frequency plane images, different pixels can have differing total bandwidths or effective frequencies. This effect is most apparent at the extremes in latitude of each image where contributions are predominantly from lower frequencies (see Fig. 3). To enable these effects to be taken into account in future data analysis we provide corresponding images of the effective central frequency and total bandwidth for each zeroth moment image as part of our DR. In general, the zeroth moment images have largely constant effective frequencies and bandwidths of 1293 and 672 MHz for Galactic latitudes $|b| \leq 1.^\circ 1$ (except near some bright sources as described below). These values steadily decrease towards the edges of the zeroth moment images as the higher frequency planes do not contribute to the zeroth moment, reaching values of 908 and 43 MHz, respectively, at the extremes (i.e. where only the first 908 MHz frequency channel is present). Caution must also be taken near bright emission where flagging of particular channels or regions may also reduce the effective frequency and bandwidth of the moment zero images near bright sources.

Table 1. Central frequencies and bandwidth of the 14 fractional bandwidth flux-density images contained in the SMGPS data cubes. Note that channels 7 and 8 are completely flagged throughout all data cubes due to persistent radio frequency interference from GPS satellites.

Channel no.	Central frequency (MHz)	Bandwidth (MHz)
1	908.142	43.469
2	952.446	43.469
3	996.751	43.469
4	1043.563	48.484
5	1092.884	48.484
6	1144.712	53.500
7	1199.048	53.500
8	1255.892	58.516
9	1317.751	63.531
10	1381.700	62.695
11	1448.157	68.547
12	1520.049	73.562
13	1594.446	73.563
14	1656.724	49.320

4.3 Flux-density calibration

In this section, we assess the accuracy of the flux densities extracted from the SMGPS by comparing to the JVLA THOR survey (Beuther et al. 2016). THOR covers a similar observed frequency range to the SMGPS and, in particular, the 1.31 GHz channel of THOR is close in frequency to the 1.29 GHz median effective frequency of the MeerKAT GPS zeroth moment images. The SMGPS observations are tied to the primary flux calibrator PKS B1934 − 638, whereas the JVLA THOR observations are tied to the JVLA primary flux calibrator 3C 286 (Beuther et al. 2016; Wang et al. 2020) with the two calibrators being tied to the same flux-density scale by Reynolds (1994). Comparing the two surveys thus enables an independent measurement of the systematic calibration errors between JVLA and MeerKAT.

Samples of bright (S/N $\geq$ 10), isolated (separated by at least 1 arcmin from the nearest neighbour) point sources were extracted from the THOR catalogue given in Wang et al. (2020), and a catalogue of SMGPS point sources was constructed by running the Aegean algorithm (Hancock et al. 2012) on the zeroth moment images. The isolation constraint was to preferentially select radio sources that were not associated with extended complexes and for which the flux densities could be determined more accurately. We restrict our analysis to point sources in THOR and SMGPS to ensure that we are comparing like-for-like flux densities. The THOR catalogue contains only peak brightness values in Jy beam^{-1}, but for point sources this is also equal to their integrated flux density in Jy.

The SMGPS and THOR catalogues were then cross-matched against each other with a matching radius of 2 arcsec. We made no attempt to correct for any variability between THOR and SMGPS epochs (THOR was observed during 2012–2014 and SMGPS during 2018–2020) or spectral index variations between the 1.31 and 1.29 GHz effective observing frequencies (which would amount at most to ∼2 per cent for the most extreme spectral indices).

Fig. 4 shows a plot of the THOR 1.31 GHz peak flux density against the corresponding SMGPS 1.29 GHz peak flux density, together with the line of equality and a best-fitting regression. We use an orthogonal distance regression to take into account the errors in both THOR and SMGPS peak flux densities and carry out the fitting in log–log space to avoid bright sources dominating the fit. As can be seen in Fig. 4, the relationship between the THOR and SMGPS peak flux densities is linear and close to $y = x$, deviating only at the level of a few per cent. There is increasing scatter towards lower flux densities, which may be due to the presence of uncorrected negative bowls in the SMGPS images. THOR includes zero-spacing information from Effelsberg 100-m single-dish mapping and is thus less affected by negative bowls. Alternatively this may indicate source variability between the observation epochs of THOR and SMGPS. The dominant constituent of the sample at ∼mJy flux densities are likely to be radio galaxies (Condon 1984; Anglada et al. 1998; Hoare et al. 2012) of which active galactic nuclei are well known to be variable on time-scales from minutes to years (Dennett-Thorpe & de Bruyn 2002). The increased scatter at low fluxes could be due to intrinsic source variability, particularly as our isolation and flux constraints may have led to a selection bias toward these source types.

In order to check the latter hypothesis we analysed subsets of the THOR and SMGPS samples, selected to be known UC H II regions from the CORNISH survey (Hoare et al. 2012; Urquhart et al. 2013). UC H II regions are known to be variable, but not on the subdecade time-scale between THOR and SMGPS measurements. The UC H II subsample again shows a close to linear relationship, but with a much smaller RMS scatter (see Fig. 4), confirming the hypothesis that much of the scatter in the larger sample is due to intrinsic source variability. For the UC H II subsample the intrinsic scatter in the relation between THOR and SMGPS flux densities is around 4 per cent and so we consider this to be the flux calibration uncertainty of the SMGPS.

4.4 Astrometric accuracy

In Section 2, we outlined two issues that could affect the astrometric accuracy of the data cubes and images (timing and frequency labelling errors, and incorrect calibrator positions). In this section, we investigate the astrometric accuracy of the SMGPS both through an internal cross-comparison and comparisons with CORNISH (Hoare et al. 2012), CORNISH-South (Irabor et al. 2023), and the International Celestial Reference Frame (ICRF; Charlot et al. 2020) catalogues.

In summary, we find that the astrometry of the SMGPS is accurate to an overall level of ∼0.″5, with possibly a small systematic offset of around 0.″1–0.″3. The positions of individual sources and particularly sources at high or low Galactic latitude in those mosaics affected by timing and frequency errors may be affected up to ∼1.″5 (19 per cent of the SMGPS FWHM resolution). Users who require much greater astrometric precision are advised to take particular care with their analysis.

4.4.1 Timing and frequency labelling errors

One of the main sources of astrometric error in the SMGPS is due to a timing and frequency labelling error of 2 s of time and half a channel of frequency. This results in an apparent rotation of each affected pointing image of up to 2 arcsec at the edge of the image. The affected data were the earliest data to be taken and lie between longitudes of 320° and 358°. Collecting the affected pointings into mosaics is expected to mitigate the errors due to the low weight placed on the edges of each individual pointing. We investigate these potential errors using the G321.5 mosaic, which was processed twice – once with the timing and frequency errors uncorrected and once with the errors corrected. Comparing the positions of point sources in both versions of this mosaic allows us to quantify the potential astrometric error resulting from this effect.

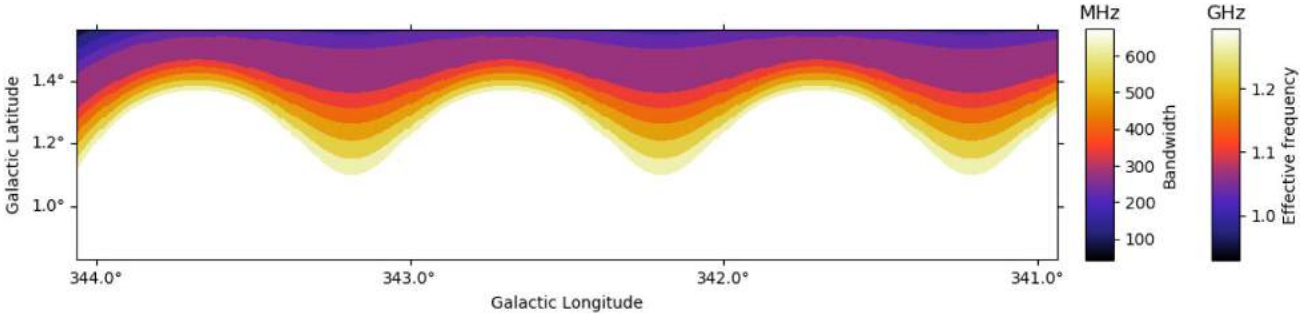

Figure 3. A portion of the G342.5 mosaic to illustrate the variation in effective bandwidth and frequency of the zeroth moment images caused by the variation in the primary beamwidth.

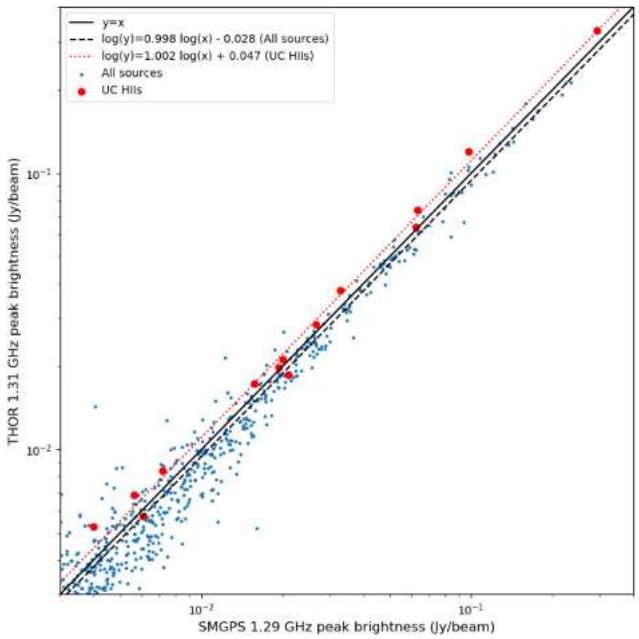

Figure 4. A comparison of the flux densities of isolated point sources from the SMGPS and THOR surveys (at 1.29 and 1.31 GHz, respectively). Each survey catalogue was filtered to retain only sources with S/N > 10. The line of equality is shown by a solid black line, the best orthogonal distance regression fit to all sources by a dashed line, and the corresponding fit to the UC H II region subsample by a dotted line. The values for the slopes and intercepts derived from the regressions are shown in the figure label.

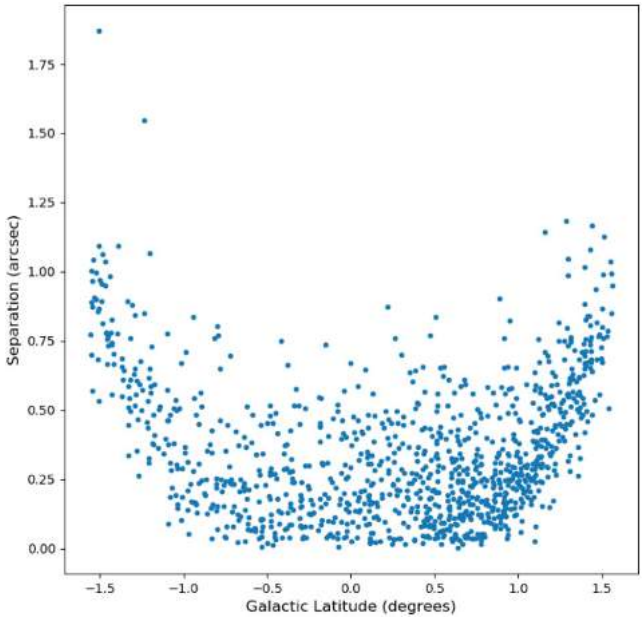

Figure 5. Angular separation of bright point sources on the timing and frequency corrected mosaic G321.5 from their apparent positions on the corresponding uncorrected mosaic, plotted against Galactic latitude. A small systematic offset at the high latitude edges of the mosaics can be seen, but is ≤ 2 arcsec even at the extremes.

Aegean (Hancock et al. 2012) catalogues of the corrected and uncorrected G321.5 mosaics were cross-matched with a maximum radius of 8 arcsec. Each catalogue was pre-filtered to contain point sources with an S/N ratio greater than 10 to reduce the intrinsic positional uncertainty. Fig. 5 shows the separation between matched point sources plotted against Galactic latitude. As can be seen the overall effect of the timing and frequency errors is small, with a median source separation of 0.″3. As expected, the source separation increases towards the high and low latitude edges of the mosaics where the mosaic mostly depends upon a single pointing. However, even at its most extreme value the positional shift resulting from the timing and frequency error – which affects only the data in the longitude range 320°–358° – is less than 1.″9.

4.4.2 Cross-comparisons with CORNISH, CORNISH-South, and the ICRF

We estimate the overall astrometric accuracy across the entire SMGPS survey by comparing to the CORNISH/CORNISH-South surveys (Hoare et al. 2012; Irabor et al. 2023) and a sample of sources drawn from the ICRF (third realization; Charlot et al. 2020).

Aegean catalogues of isolated (by more than 1 arcmin) point sources from the SMGPS were cross-matched against similar isolated point sources taken from the reliable (S/N $\geq$ 7) catalogues of 5 GHz point sources drawn from the CORNISH (Hoare et al. 2012) and CORNISH-South (Irabor et al. 2023) surveys. The point sources were selected to be isolated to avoid confusion with nearby objects and in addition the CORNISH and CORNISH-South catalogues were pre-filtered to only include source types expected to have similar compact or point-like morphologies at the different frequencies of SMGPS and CORNISH/CORNISH-South (UC H II regions, PNe, and radio stars). This latter point takes into account the much greater sensitivity of SMGPS to the unresolved lobes of radio galaxies, which

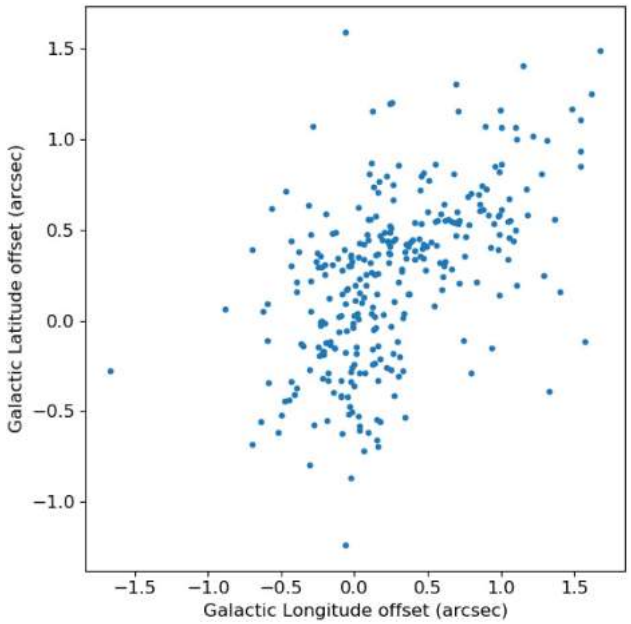

Figure 6. Angular separation between the positions of matched sources in the SMGPS and CORNISH/CORNISH-South surveys. To avoid confusion from lobes of radio galaxies that are preferentially detected by MeerKAT, the CORNISH sources are pre-filtered to only contain sources that are expected to have similar morphologies at all frequencies, that is, UC H II regions, PNe, and radio stars.

can introduce a systematic shift in the measured positions of these sources as compared to CORNISH/CORNISH-South.

Fig. 6 shows a scatter plot of the Galactic longitude (l) and Galactic latitude (b) offsets between corresponding SMGPS and CORNISH/CORNISH-South point sources. Clearly there is an element of minor systematic error in the positions as the points are not symmetric around an (l, b) offset of (0, 0). The median offset in (l, b) is (0.″16, 0.″30) with a standard deviation of 0.″5 in both l and b.

In addition to CORNISH/CORNISH-South, we also conducted an examination of the positional offsets between the SMGPS catalogue and 28 ICRF sources found within the survey area. These 28 sources are relatively bright in the SMGPS (median 1.29 GHz flux density of 1.3 Jy), so the statistical uncertainty in the MeerKAT position determinations is small. The sources were chosen for the ICRF by virtue of being compact on milli-arcsecond scales, and generally do not have any structure on the scale of MeerKAT's resolution of 8 arcsec which might affect the position determination. Since the ICRF constitutes the most accurately known set of astronomical positions, they are an ideal additional check of the absolute astrometry in the MeerKAT images.

We therefore compared our point-source catalogue positions with those of the ICRF3[7] sources that were included in our fields, which we list in Table 2.

We found that the MeerKAT catalog positions differed from the ICRF3 ones by <1.″5. The largest offset was for ICRF J193629.3 + 224625, for which the MeerKAT catalog position was (−0.″8, +1.″2) from the ICRF position in (l, b). Over all 28 sources, the mean and RMS deviation between our catalogue positions and the ICRF ones were −0.″21 ± 0.″35 in l and −0.″13 ± 0.″40 in b. This is consistent with the results as found from the comparison with CORNISH/CORNISH-South, lending confidence that the positions of SMGPS sources are known to an RMS accuracy of ∼0.″5.

[7] http://hpiers.obspm.fr/icrs-pc/newwww/icrf/index.php

Table 2. ICRF sources in the SMGPS.

J080125.9 − 333619	J080644.7 − 351941	J082804.7 − 373106
J093333.1 − 524019	J120651.4 − 613856	J135546.6 − 632642
J151512.6 − 555932	J163246.7 − 455801	J171738.6 − 394852
J173657.8 − 340030	J174317.8 − 305818	J174423.5 − 311636
J175151.2 − 252400	J175526.2 − 223210	J183220.8 − 103511
J184603.7 − 000338	J185146.7 + 003532	J185535.4 + 025119
J185802.3 + 031316	J190539.8 + 095208	J192234.6 + 153010
J192439.4 + 154043	J193052.7 + 153234	J193450.2 + 173214
J193510.4 + 203154	J193629.3 + 224625	J194606.2 + 230004
J194933.1 + 242118		

4.5 Spectral indices

The ability to derive spectral indices from images made from interferometer data depends on the array adequately sampling all of the relevant size scales across the entire observing band. This causes problems in the GP with structure on a huge range of scales.

In the construction of the 'dirty' images zeros are substituted for unsampled visibilities. Since the region around the origin is almost never sampled due to the physical constraints of moving antennas, this results in a dirty image which in the average is zero. This leaves negative regions balancing positive ones. Deconvolution (here CLEAN) is a technique for interpolating over regions of the *uv* plane which were not sampled. Deconvolution has its limits.

The largest scales which can be imaged are limited by the *uv* coverage of the shortest baselines measured in wavelengths. With the 2:1 frequency coverage of MeerKAT *L* band this means that the data at the bottom of the band can image structures of twice the size of data at the top of the band. Alternatively, the portion of the image at the bottom of the band can recover a significantly higher fraction of the flux density for resolved sources than at the top end of the band. Deconvolution helps with this problem but, if the extent of the feature is significant, will not eliminate it. A naive spectral index derived from such data can appear much more negative than reality.

The difference in largest structure sampled across the band can be greatly reduced by using an 'inner' taper (Cotton et al. 2020) to equalize the short baseline coverage across the band. This leads to better estimates of in-band spectral index but comes at a cost of filtering out the largest scale structures which are only visible at the bottom of the band. This seems like a poor trade-off for the GP.

The CLEAN used for the data presented here is relatively shallow and used only point components. No inner *uv* taper was applied. A deeper CLEAN using multiple scales (or the equivalent) combined with an inner taper to equalize the *uv* coverage could result in more accurate spectral indices for the surviving structures. The ultimate fix is to include filled aperture (e.g. large single dish) data. Such exercises are deferred to future DRs.

Although the SMGPS DR includes in-band spectral index values, α, determined by fitting a power law to the brightness in the frequency-resolved planes, these values of α should only be used with considerable caution. As described above, near regions of bright emission the effective zero level in the images can be significantly offset from zero Jy beam^{-1}, usually being negative. This 'zero offset' is strongly frequency dependent.

As a consequence, the spectral index fitted to the layers in the cubes, and present as layer 1 in the 'refit' cubes, can be significantly biased. For a better estimation of the spectral index, some frequency-

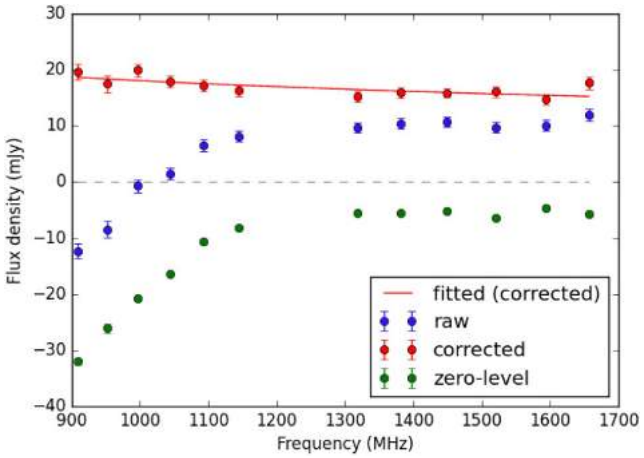

Figure 7. An example of the effect of zero levels on the determination of spectral indices: the spectrum for the candidate PWN around PSR J1208 − 6238 (see Section 5.3 and Fig. 13 for further details on this object). The candidate PWN is a relatively compact source, about 23 arcsec (∼3 beamwidths) in radius and with a total flux density of ∼16 mJy. The blue points show the raw flux density in a region with equivalent radius 23 arcsec around the candidate PWN. The green points show the flux density due to the zero level, which was estimated by taking the mean brightness from an approximately annular region just around the putative PWN. The red points show the difference of the two, or the corrected flux density, and the red line shows the fitted power-law spectrum with $S_\nu = 16.3\ (\nu/1360\,\mathrm{MHz})^{-0.33}$ mJy. The grey dashed line shows flux density 0 for reference. The plotted uncertainties include both statistical and systematic contributions.

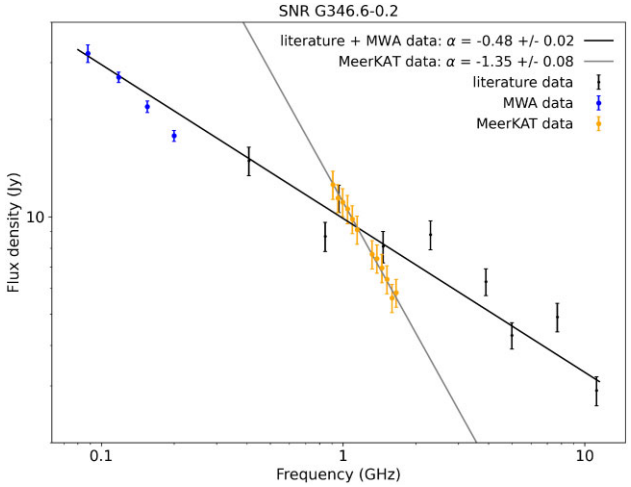

Figure 8. Spectrum of the SNR G346.6 − 0.2. The thick black line is the fit to literature values (Trushkin 1999; Hurley-Walker et al. 2019a). Yellow points are the SMGPS values, with the thin grey line showing the corresponding fit. The two fits intersect approximately at the central frequency of the MeerKAT band, but have different spectral indices.

dependent estimate of the local 'zero level' near the source of interest should be made. For more accurate values, a deeper, multiresolution CLEAN using an inner *uv* taper should be carried out.

As an example, we show in Fig. 7 the spectrum of some emission around PSR J1208 − 6238, which is a new candidate pulsar wind nebula (PWN) discovered in the SMGPS (for further details, see Section 5.3 and Fig. 13a below). As can be seen in the figure, the zero levels are strongly frequency-dependent, and therefore the correction for the zero level strongly affects the determination of the spectral index.

We attempted a correction for the zero levels by fitting, for each sub-band independently, a mean zero-level brightness to an approximately annular area selected to be apparently devoid of real emission around the source, and then subtracted the mean brightness value in this annular region from the source brightness. A power-law function ($B_\nu \propto \nu^\alpha$) fitted by least-squares to the resulting flux densities (brightness integrated over the source region) results in a good fit, and a credible spectral index of −0.33 which is in the expected range for a PWN.

The determination of local zero level depends on the dimension of the source. For extended sources, the fluctuations of the zero level in the image can be relatively high, depending on the brightness of the target source and of any other sources around it that were not adequately CLEANed. The fluctuations in the zero level at any point in the image are often due to several nearby sources and therefore depend significantly on the wavelength, and can have a significant effect on the slope of the spectrum (as seen in Fig. 7).

As further examples, we selected three SNRs several arcminutes across, namely G340.6 + 0.3 (diameter of 6′.2), G346.6 − 0.2 (8 arcmin), G344.7 − 0.1 (8 arcmin), with known spectral indices $\alpha = -0.35$, −0.50, and −0.53, respectively (Trushkin 1999). From the SMGPS mosaic cubes, for each frequency plane, we compute the integrated flux density inside a circular region with radius equal to the maximum radius of the source. First, we subtracted the average brightness computed in an annular region just outside the source. Then, we did a linear least-squares fit of $\log S_\nu$ to $\log \nu$ to find α. The nominal SMGPS in-band spectra are quite steep: $\alpha = -0.67$, −1.35, and −1.65 for the three SNRs, respectively. For all three SNRs, the SMGPS in-band spectra are notably steeper than those from the literature, indicating that for these three sources, with diameters between 6 and 8 arcmin, simple estimation of a constant zero level from a region just outside the source is not adequate.

Despite these issues, the flux densities computed for the centre of the SMGPS band are in good agreement with the literature values. For example, measurements of the SNR G346.6 − 0.2, shown in Fig. 8, clearly show that, near the centre of the SMGPS band, the SMGPS flux-density measurements agree with the spectrum obtained from the literature (Trushkin 1999; Hurley-Walker et al. 2019a). However, the slope corresponding to the SMGPS values is notably steeper than that determined over a much wider frequency range from literature values.

For point-like and compact sources, smaller than a few synthesized beam areas, the local zero-level brightness does not vary much over the source, and should be reliably estimated from the region immediately around the source. The spatial and brightness scales on which the zero level varies depends on the complexity of the surrounding field, and there is no general rule to estimate the spatial scale for which they become problematic, but in general they can be more reliably estimated for smaller sources.

To try to determine for which source size the SMGPS in-band spectral indices may be reliable, we computed the SMGPS in-band α for a sample of sources with angular diameters ranging from 7 to 1000 arcsec. We selected a number of resolved sources of three different classes, SNRs (eight, including the three mentioned above), H II regions (11) and unclassified sources (14), all of them with approximately circular morphology. We plot the resulting nominal in-band values of α against the source size in Fig. 9. There is a clear correlation between the SMGPS in-band α and the angular size. For small diameters, the values of α are broadly within the expected range between −1 and 0, but as the angular size increases, the in-

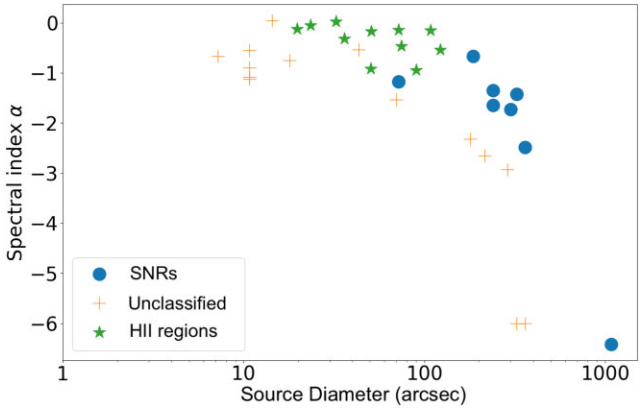

Figure 9. SMGPS nominal in-band spectral indices as a function of the angular diameter of the source for three classes of resolved sources with relatively circular morphologies.

band α values become quite negative, with $\alpha < -3$ determined for sources >300 arcsec. Such values are unphysical for these source classes, and the SMGPS values are unreliable here.

In conclusion, the in-band spectral index values should be interpreted very cautiously. The effect of the frequency-dependent local zero levels in the images must be taken into account unless the brightness of the source is much larger than the zero-level offsets. For small sources, the zero levels may be reliably estimated from the region just around the source, but for larger sources, the zero-level offsets are anticorrelated with the actual source brightness, and the derived in-band spectra can be significantly in error, most often being too steep. It appears that for the current DR, estimation of α should not be attempted for sources with diameters $\gtrsim 1$ arcmin, and even for smaller sources great care should be taken with estimation of zero levels.

5 GALACTIC SCIENCE HIGHLIGHTS

In this section, we present some of the science highlights from the survey to illustrate the data quality, scientific results, and the different source populations discovered in the SMGPS.

5.1 Radio filaments

Filamentary structures are ubiquitous constituents of the ISM across a variety of size scales and environments, from low-density dust cirrus (e.g. Low et al. 1984; Bianchi et al. 2017), to neutral atomic H I filaments (e.g. Kalberla et al. 2016; Kalberla, Kerp & Haud 2020; Soler et al. 2020), and both quiescent and star forming filaments in high-density dust and molecular gas (e.g. André et al. 2014; Li et al. 2016; Schisano et al. 2020). In the ionized ISM, an intriguing kind of filamentary phenomenon has been identified towards the Galactic Centre (Yusef-Zadeh, Morris & Chance 1984; Yusef-Zadeh, Hewitt & Cotton 2004; Barkov & Lyutikov 2019; Heywood et al. 2019, 2022) and Orion (Yusef-Zadeh 1990). These so-called non-thermal filaments (NTFs) are highly linear with large aspect ratios (with many of the longest aligned perpendicular to the GP), are inherently non-thermal in nature, and are highly magnetized with intrinsic B field vectors aligned parallel to their lengths (Lang, Morris & Echevarria 1999). A consensus is yet to be reached on the means of formation of these NTFs, with many proposed theories including both external and *in-situ* acceleration of relativistic particles (e.g. Yusef-Zadeh et al. 1984, 2022a; Morris & Serabyn 1996; Rosner & Bodo 1996; Barkov & Lyutikov 2019; Coughlin, Nixon & Ginsburg 2021). Due to a lack of NTFs observed elsewhere in the Galaxy, it has so far been generally agreed that they are structures that occur in the uniquely extreme and energetic environment of the Galactic Centre.

The SMGPS images reveal a plethora of complex, elongated, filamentary structures. Some are associated with extended sources such as SNRs (see Section 5.2) and H II regions, while others appear to be isolated. We implemented a semi-automated method for their identification in as consistent a way as possible across the survey area. A high-pass filter was applied to the moment zero images for the removal of large-scale diffuse emission, in effect increasing the contrast of compact sources and the ridges/spines of narrow structures against the local background (e.g. Yusef-Zadeh et al. 2022b). The filtered images were thresholded to create a mask of all emission brighter than three times the local background RMS brightness. The masks were segmented based on their shape by calculation of their principal moments of inertia (using the *J*-plots algorithm; Jaffa et al. 2018), and only the most elongated structures (with aspect ratios >4) were selected. A final visual inspection of all extracted structures allowed removal of any clear artefacts such as strong sidelobe features. We emphasize that our method does not pick up structures connected to diffuse or extended emission, because we are choosing only the brightest, isolated, and most elongated structures in a semi-automated fashion.

With this method, we identify a population of radio filaments across the GP. The full catalogue will be presented elsewhere. As an example, we present here a subsample of 21 filaments from the G312.5 tile ($311^\circ < l < 314^\circ$). We show both the unfiltered and filtered images of this region in Figs 10 (a) and (b), and list the filament properties in Table 3.

The filaments in this region appear with two distinct morphologies: (i) a bundle of filaments oriented at an angle to the GP, and (ii) relatively isolated filaments oriented almost perpendicular to it. Concerning the former, Cohen & Green (2001) noted the presence of 'large-scale braided filamentary structures' in the Molonglo Galactic Plane Survey data (MOST, Green et al. 1999) observed at 843 MHz (see Fig. 10c). It was further noted by Cohen & Green (2001) that these filaments appear to be coincident with similarly braided 'tendrils' of 8.3 μm mid-IR (MIR) emission observed with MSX (see Fig. 10d; Price et al. 2001), likely signposting emission from polycyclic aromatic hydrocarbons; this strongly suggests that these radio filaments are thermal in nature. Cohen & Green (2001) posited that the alternating pattern of MIR-ridge to radio-ridge (see Fig. 10d) suggests that the filaments are limb brightened sheets of emission at the edge of a large-scale bubble with diameter $>1^\circ$ centred above $b = 0.^\circ5$, though this remains uncertain. With an angular resolution of 46 arcsec, Cohen & Green (2001) were unable to resolve the filaments, nor distinguish whether the radio emission was as intricate as that seen in the MIR. With the 8 arcsec angular resolution of SMGPS, we give a first estimate for the resolved width of these filaments in Table 3, and confirm that the radio emission structure is indeed highly complex – intertwining tendrils of radio emission are indeed interspersed with MIR emission on the south-west side of the bundle, whilst the filaments on the north-east side of the bundle appear unrelated to MIR emission (Fig. 10d). Thus, as they are on the whole likely thermal, these braided filaments are fundamentally different in nature to the NTFs identified towards the Galactic Centre (e.g. Heywood et al. 2019). Concerning the isolated filaments oriented almost perpendicular to the GP, we identify three highly elongated filaments to the north-west of the filament bundle, and four shorter filaments to the north-east. Despite the three longest filaments being, at least retrospectively, noticeable in the 843 MHz

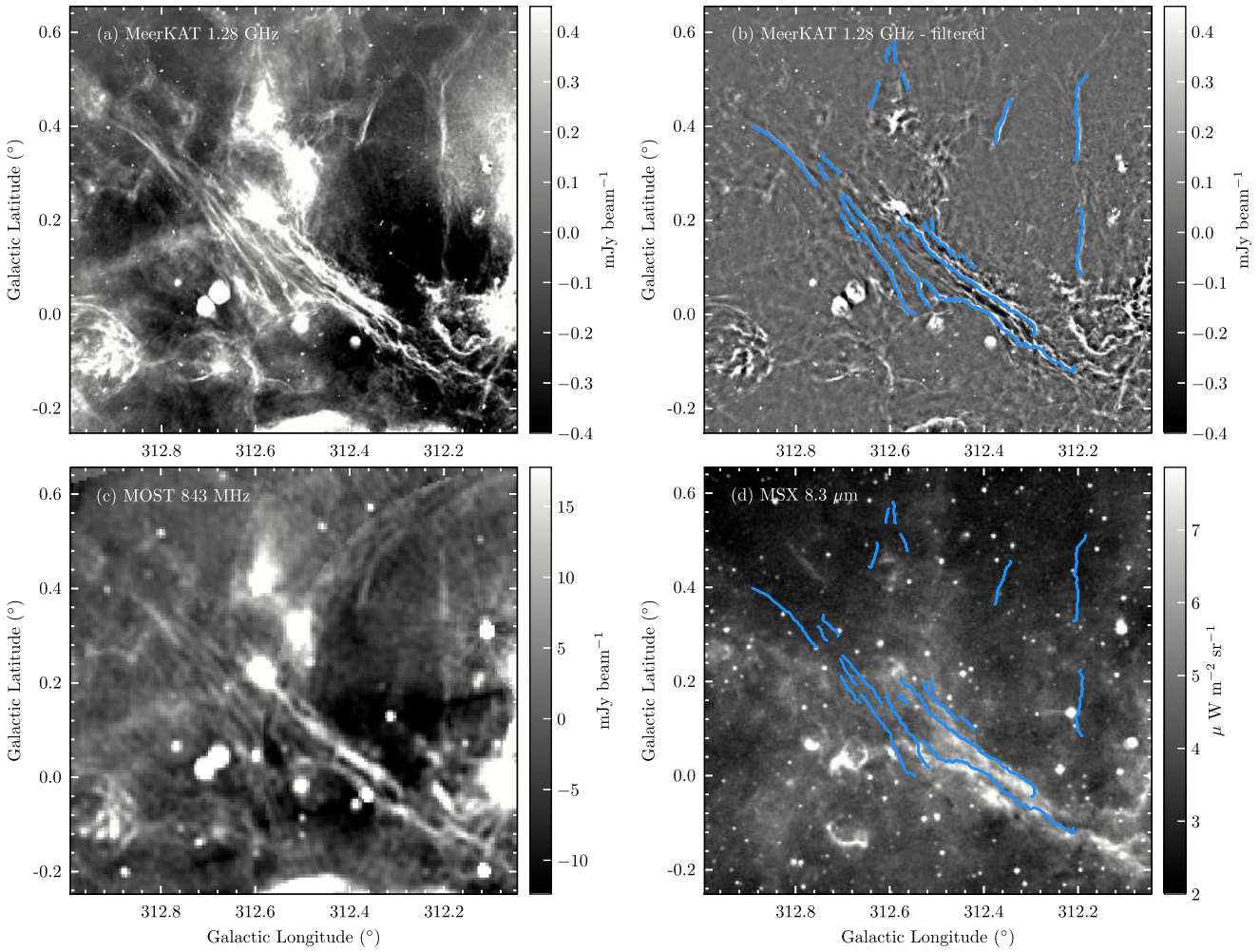

Figure 10. Zoomed-in view of a filamentous region in the $311^\circ < l < 314^\circ$ SMGPS tile showing (a) the 1.28 GHz MeerKAT image (with 8 arcsec angular resolution), (b) the high-pass filtered MeerKAT image (i.e. with removal of contamination from foreground/background emission), (c) the 843 MHz MOST image (Green et al. 1999, with 46 arcsec resolution), and (d) the 8.3-μm MSX image (Price et al. 2001, with 20 arcsec resolution). The spines of 21 identified filaments (where the spine traces the high-intensity crest/backbone of the filament) are marked in blue in panels (b) and (d), and the colour scale in all panels is shown on a linear scale.

MOST image (Fig. 10c) they were not discussed by Cohen & Green (2001). All seven of these filaments appear to be unrelated to 8.3 μm MIR emission (Fig. 10d), strongly suggesting they are non-thermal in nature.

Due to the limitations discussed in Section 4.5, we are at this point unable to derive reliable spectral indices for these extended filamentary structures, or their polarization properties, since polarized data reduction was not done for the G312.5 tile. Though the braided, MIR-associated, likely thermal filaments in the bundle are fundamentally different in nature to NTFs, the isolated filaments identified here may be good candidates for the first NTFs identified outside the Galactic Centre region. Their highly linear nature and the fact that their widths are resolved (see Table 3) are reminiscent of the Galactic Centre population of NTFs. The apparent lack of coincident MIR emission towards these isolated filaments is also suggestive of a non-thermal nature. Unlike many NTFs in the Galactic Centre, the isolated filaments presented here do not appear to have point sources along their lengths, however they do reside in a region filled with bubbles, H II regions and SNRs, and therefore may possibly be examples of externally driven NTFs. These results raise the possibility that the NTF phenomenon might be more prevalent across the Galaxy than previously appreciated. A forthcoming investigation of filamentary structures in the full SMGPS DR will address this topic in detail.

5.2 Supernova remnants

SNRs emerge in the aftermath of most supernova explosions (SNe). SNe are the end stage of massive stars, and the birthplace of neutron stars and stellar-mass black holes. They also inject a substantial amount of energy into the ISM, as well as being the major contributors to the chemical enrichment of the ISM.

In an SN explosion, typically several solar masses of material are ejected from the star, and plough outward through the circumstellar medium, typically the stellar wind of the progenitor star, or the ISM. In so doing, they produce strong shocks which accelerate particles to relativistic energies and amplify the magnetic field, the combination of which produces non-thermal radio emission.

Radio emission is therefore one of the important hallmarks of SNRs, and is most often the way that they are identified. The most

Table 3. Observed properties of a subset of filaments identified in the $311^\circ < l < 314^\circ$ SMGPS tile.

Centroid coordinates[a]		Peak intensity	Length	Width[b]	Aspect ratio	PA[c]	*J* moments[d]		MIR[e]	Bundle[f]
l (°)	b (°)	(mJy beam^{-1})	(arcmin)	(arcsec)		(°)	J_1	J_2	assoc.	versus isolated
312.367	−0.026	3.27	27.3	9.0	183.0	− 60.0	0.59	−0.76	Y	Bundle
312.434	0.078	1.24	25.9	25.4	61.0	− 48.0	0.59	−0.81	Y	Bundle
312.602	0.082	0.49	13.9	12.3	68.0	− 33.0	0.55	−0.82	Y	Bundle
312.563	0.093	1.82	11.8	22.6	31.0	− 31.0	0.70	−0.78	Y	Bundle
312.196	0.155	0.40	10.0	26.8	22.0	− 1.0	0.77	−0.84	N	Isolated
312.434	0.112	0.41	2.7	5.8	27.0	− 41.0	0.60	−0.78	Y	Bundle
312.495	0.156	0.94	7.2	11.8	37.0	− 42.0	0.63	−0.83	Y	Bundle
312.571	0.163	0.37	1.9	8.3	14.0	− 52.0	0.75	−0.78	Y	Bundle
312.656	0.204	0.39	9.6	16.3	35.0	− 41.0	0.55	−0.66	Y	Bundle
312.685	0.182	0.39	4.8	15.4	19.0	− 36.0	0.45	−0.69	Y	Bundle
312.511	0.191	0.24	1.5	9.9	9.0	− 14.0	0.60	−0.74	Y	Bundle
312.690	0.220	0.48	4.2	11.9	21.0	− 31.0	0.17	−0.92	Y	Bundle
312.819	0.343	0.38	11.9	21.2	34.0	− 47.0	0.72	−0.75	N	Bundle
312.743	0.302	0.22	2.5	16.4	9.0	− 34.0	0.73	−0.80	N	Bundle
312.727	0.319	0.35	3.9	15.0	16.0	− 34.0	0.59	−0.87	N	Bundle
312.201	0.419	0.57	13.0	23.7	33.0	8.0	0.82	−0.84	N	Isolated
312.362	0.410	1.04	6.6	24.1	16.0	19.0	0.82	−0.82	N	Isolated
312.632	0.467	0.22	4.0	17.0	14.0	18.0	0.52	−0.81	N	Isolated
312.568	0.495	0.29	2.6	16.3	10.0	− 22.0	0.57	−0.83	N	Isolated
312.590	0.559	0.19	3.2	14.2	13.0	− 7.0	0.36	−0.83	N	Isolated
312.606	0.553	0.22	2.1	15.5	8.0	10.0	0.57	−0.72	N	Isolated

Notes. [a]Centroid position of the filament spine.
[b]Deconvolved FWHM of a Gaussian fitted to the mean transverse intensity profile of the filaments.
[c]Mean position angle of the filament spine, measured from Galactic North (where PA=0°), with positive values in the clockwise direction.
[d]Derived from the principal moments of inertia of the structure masks (using the *J*-plots algorithm; Jaffa et al. 2018). The *J* moments describe the shape of the object; positive J_1 and negative J_2 values together denote elongated, filamentary-like structures.
[e]A flag noting whether the filament is coincident with 8.3 μm MSX emission (Y) or not (N).
[f]A note describing whether the filament is isolated, or belongs to the bundle of braided filaments described in the text (see Section 5.1).

complete current catalogue as of 2022 is that of Green,[8] which is an updated version of Green (2019) containing 303 SNRs.

Studies of SNRs in the radio are often limited by either resolution or surface-brightness sensitivity. MeerKAT's high sensitivity and resolution, alongside superb image fidelity, therefore make it an ideal instrument for studying known SNRs. Also, its southern location allows a view of the central parts of our Galaxy, where many SNRs are expected due to the high stellar density. There is a long-standing tension between the ≈300 currently established Galactic SNRs, and the ≈1000–2000 that may be expected (Li et al. 1991; Tammann, Loeffler & Schroeder 1994; Gerbrandt et al. 2014; Ranasinghe & Leahy 2022). The large area coverage of the SMGPS allows a more detailed study of many known SNRs, and should enable the discovery of many new SNRs in a good fraction of the Galaxy to lower surface brightness than previous wide-area surveys.

5.2.1 *Known SNRs*

Approximately 200 known SNRs are imaged in the SMGPS. In Fig. 11, we show images for 12 of them. These were selected to show examples of the ways in which the SMGPS provides a markedly improved view over previously available radio images, in a variety of environments. For example, in several of the images the full(er) extent of the SNR becomes apparent, owing to improved surface-brightness sensitivity; in many others, fine scale filamentary features become apparent where previously none were known. A further example is given in Appendix A, where we present a full polarization analysis of the SNR W44.

[8]See https://www.mrao.cam.ac.uk/surveys/snrs.

SNR G11.1 − 0.7. The SMGPS image shows a complex structure ∼15 arcmin in diameter, brighter to the Galactic NE, with a number of filaments, but not clearly a shell. Much lower resolution and dynamic range images at 327 and 1465 MHz were published in Brogan et al. (2004), which do not show the extent or the filamentary nature of the emission.

SNR G24.7 − 0.6. Centred at l, $b = 24\overset{\circ}{.}9$, $-0\overset{\circ}{.}6$, approximately circular in outline with radius ∼9 arcmin but fading to the Galactic SSE, this SNR has an area of filamentary emission. It is somewhat edge brightened, and possibly a shell. Superposed, and perhaps interacting with this, is a dominant filamentary bundle running from Galactic NNE to SSW, which overlaps and curves around the western edge of the possible shell, that is likely identified as PMN J1838 − 0734 (Griffith et al. 1995). The best published radio image seems to be that of Dubner et al. (1993, VLA, Very Large Array; resolution ∼50 arcsec), which gives only the vaguest hint of the possible shell component.

SNR G41.5 + 0.4. Roughly circular in outline, ∼16 arcmin in diameter, with an enhancement both near the centre and towards the Galactic ESE (identified as [ADD2012] SNR 21 in Alves et al. 2012 and RRF 305 in Reich, Reich & Fuerst 1990). A VLA 332-MHz image was presented in Kaplan et al. (2002), with resolution ≈50 arcsec. The SMGPS image reveals numerous loops and filaments throughout. Kaplan et al. (2002) had suggested a possible central PWN, $\sim 3' \times 1\overset{'}{.}5$ in extent, but with our improved image fidelity it is possible that this is simply a centrally located brighter complex of loops and filaments.

SNR G289.7 − 0.3. The only previously published image seems to be from MOST at 843 MHz (Whiteoak & Green 1996), with much lower resolution (43 arcsec) and dynamic range than from SMGPS. Although the earlier image reveals the ∼14 arcmin extent of the

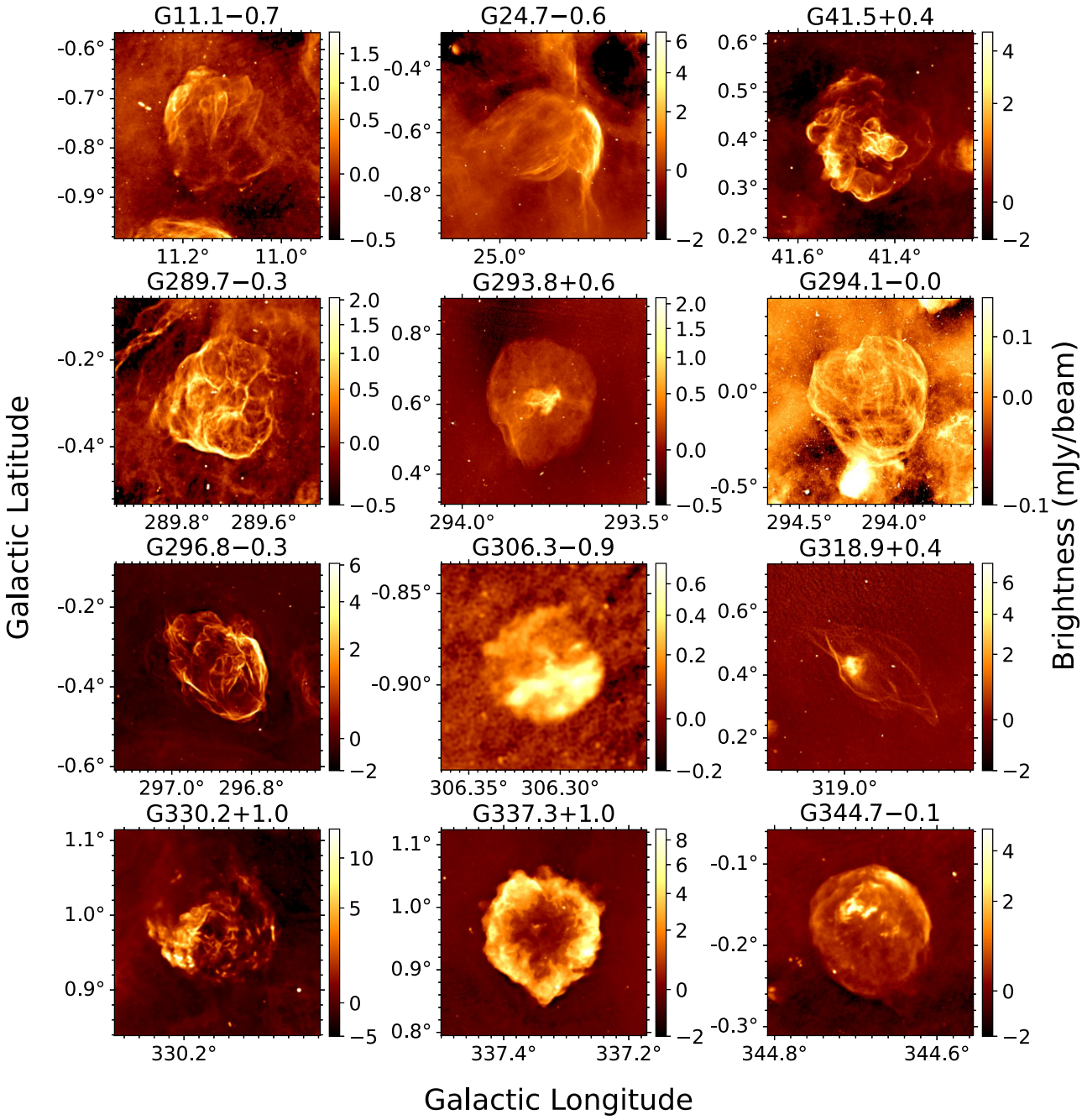

Figure 11. SMGPS images for 12 known SNRs. Each panel is centred on the MeerKAT emission identified with the SNR and has a width of three times the identified radius. The colour scale shows brightness with a square-root stretch.

emission and some filamentation, it does not show the details of the filaments or the unusual interlocking loops seen in the SMGPS image.

SNR G293.8 + 0.6. The only previously published image seems to be that of Whiteoak & Green (1996). The emission extends over a roughly circular region of ∼20 arcmin diameter, and shows a prominent central condensation about 5 arcmin in extent, which is quite filamentary and could plausibly be a PWN. The filamentary nature of the central component was not evident in the previous image.

SNR G294.1 − 0.0. The only previously published image seems to be that of Whiteoak & Green (1996). The emission extends over a roughly circular area of ∼40 arcmin in diameter, with extensive filamentation. The SNR may be interacting with another, brighter, extended source, ∼6 arcmin × 12 arcmin in extent, which lies contiguous to the SNR to Galactic SSE, which is identified as an IR bubble, likely associated with the H II region [HKS2019] E140 (Hanaoka et al. 2019).

SNR G296.8 − 0.3. Gaensler, Manchester & Green (1998) published 1.3-GHz, ∼23 arcsec-resolution images from the Australian Telescope Compact Array (ATCA) of this SNR, which are

consistent with, but of considerably lower resolution and dynamic range than the SMGPS image. The SNR has an elongated morphology, ∼18 arcmin × 12 arcmin in overall extent, with edge-brightened filamentary structure, including interior loops. It is detected in X-rays, and has a central point-like X-ray source, 2XMMi J115836.1 − 623519 (Sánchez-Ayaso et al. 2012). We do not see any compact radio source $\gtrsim$ 100 μJy beam^{-1} at the location of 2XMMi J115836.1 − 623519.

SNR G306.3 − 0.9. A small source, only ∼3 arcmin in diameter. It is roughly circular in outline, but is not noticeably edge-brightened. It is divided into two halves along an ESE-WNW line, with the half to the Galactic S being notably brighter. The SMGPS image shows much more detail than the 5.5-GHz one (ATCA, resolution 24 arcsec) of Reynolds et al. (2013), revealing a somewhat flocculent structure, with the most prominent features being aligned approximately ESE-WNW. The same division into two halves of unequal brightness is seen in X-rays (Reynolds et al. 2013), although the detailed correspondence between radio and X-ray brightness is poor. The object is also identified in the IR as [SPK2012] MWP1G306301 − 008946, with the 24 μm emission largely lying along the outline of the radio emission region, and appearing more filamentary than the radio. It is conceivable that this source could be an H II region.

SNR G318.9 + 0.4. Unusual, elongated morphology, ∼30 arcmin × 14 arcmin in extent, with elliptical arcs, and an off-centre bright 'core'. The best published image is that of Whiteoak (1993) at 843 MHz from MOST (resolution ∼47 arcsec). The SMGPS image shows the arcs much more clearly, as well as showing that the core is relatively small at only ∼5 arcmin diameter, and has considerable internal structure, which appears quite distinct from the arcs, although the arcs are brighter near it.

SNR G330.2 + 1.0. Radio emission which is relatively circular in outline and ∼7 arcmin in diameter. It is brighter in a wedge to the Galactic SE, and has a flocculent structure throughout. An 843-MHz image from MOST (Whiteoak & Green 1996) shows the general outline, but it is at much lower resolution (∼49 arcsec) and does not show the flocculent structure visible in the SMGPS image. There is a central X-ray source, 2XMM J160103.4 − 513353, likely associated (Mayer & Becker 2021), however no compact counterpart with brightness > 200 μJy beam^{-1} is visible in the SMGPS.

SNR G330.2 + 1.0. Nearly circular, edge-brightened shell structure, ∼12 arcmin in diameter, with a possible axis of symmetry perpendicular to the GP. The best published radio images seem to be from MOST at 843 MHz (Kesteven & Caswell 1987; Whiteoak & Green 1996), which show the general shape but very little detail. Low surface brightness 'blowouts' or 'ears' are prominent in the SMGPS image, especially in the northern sector of the SNR.

SNR G344.7 − 0.1. Shell-like structure, ∼9 arcmin in diameter, brighter to the Galactic NW, with some bright interior features, somewhat to the Galactic N of the geometrical centre. The Giacani et al. (2011) 1.4-GHz radio image from ATCA and VLA data, with resolution similar to that of the SMGPS image but RMS noise approximately one order of magnitude higher, does not show the complete and almost circular outline of the radio emission.

5.2.2 *New candidate SNRs*

The SMGPS images surely contain many as-yet unknown SNRs, and indeed are an excellent tool for identifying new candidate SNRs. We did so, using a method of SNR detection similar to that of Anderson et al. (2017) and Dokara et al. (2021). The vast majority of discrete extended sources $\gtrsim$ 1 arcmin in the SMGPS images are either SNRs (whether previously known ones or new candidates) or H II regions.

We visually examined SMGPS images overlaid with the positions of H II regions from the WISE Catalogue of Galactic H II Regions (Anderson et al. 2014, hereafter the 'WISE Catalogue') to create a catalogue of extended MeerKAT radio continuum sources that cannot be explained as being previously known H II regions. For each identified source we noted its centroid and the circular radius necessary to contain the emission. For each catalogue source we then examined MIR data from *Spitzer* GLIMPSE (Benjamin et al. 2003; Churchwell et al. 2009) at 8.0 μm and MIPSGAL (Carey et al. 2009) at 24 μm for sources at $|b| < 1\overset{\circ}{.}0$ or WISE (Wright et al. 2010) 12 and 22 μm data for sources further from the GP. We removed sources from the catalogue with associated ∼ 10 μm emission surrounding ∼ 20 μm emission of a similar or complementary morphology to that of the MeerKAT radio continuum, as this morphology is associated with thermally emitting objects (Anderson et al. 2014). This process removes H II regions that are not listed in the WISE Catalogue; the remaining catalogue should contain only known SNRs and SNR candidates.

Finally, we identified previously known SNRs in the catalogue using the 2022 compilation of Green,[9] and previously identified SNR candidates using the results from Helfand et al. (2006), Green, Reeves & Murphy (2014), Anderson et al. (2017), Hurley-Walker et al. (2019b), and Dokara et al. (2021). The remaining catalogue sources are SNR candidates newly identified in the SMGPS data.

The full catalogue of ∼100 new SNR candidates will be presented elsewhere. Here, in Fig. 12, we show eight candidate SNRs from this catalogue with a variety of morphologies and in a variety of environments. We designate them by the Galactic coordinates of their estimated centre.

G10.67 − 0.38. Relatively circular shell structure, ∼2$\overset{'}{.}$5 in diameter. The region is somewhat confused, and G10.67 − 0.38 may form part of the ∼10 arcmin-diameter radio source GPA 010.68 − 0.37 identified in the Green Bank Galactic Plane survey (Langston et al. 2000). The MIR panel of G10.67 − 0.38 in Fig. 12 shows a complex of H II regions to the Galactic W. These are distinguishable from SNRs by their bright MIR emission that is spatially correlated with that of the MeerKAT radio continuum. Although this SNR candidate has faint associated 24 μm emission, it lacks the 8.0 μm emission that would be present for an H II region.

G39.04 + 0.75. Unusual structure extending over a region ∼18 arcmin in diameter, but broadly reminiscent of some SNRs as observed with MeerKAT (e.g. see G11.1 − 0.7 in Fig. 11). It is quite strongly filamentary, and there is bright condensation to the Galactic NE. Dokara et al. (2021) identified this bright condensation as SNR candidate G039.203 + 0.811 but did not discern the large region of emission to its SW seen in the SMGPS image. A feature elongated along the Galactic E-W direction lies largely separated from the main structure by ∼2 arcmin to the Galactic S, and it is not clear whether they are in fact physically related.

G259.68 − 1.23. Diffuse relatively circular structure, ∼12 arcmin in diameter, with several nearby and overlapping H II regions in its southern half.

G299.68 − 0.01. Roughly circular structure, ∼20 arcmin in diameter, not noticeably edge-brightened but very filamentary and with blowouts/extensions to the S and SE. Broadly speaking, the morphology of this SNR candidate has parallels to those of SNRs G41.5 + 0.4 and G296.8 − 0.3 as seen in Fig. 11. There is a small H II

[9] https://www.mrao.cam.ac.uk/surveys/snrs.